Catalysis Science & Technology

Accepted Manuscript

ROYAL SOCIETY OF CHEMISTRY

www.rsc.org/catalysis

Role of different coordinated Cu and reactive oxygen species on the highly active Cu-Ce-Zr mixed oxides in NH_3-SCO: A combined *in situ* EPR and O_2-TPD approach

Zhenping Qu[a+]*, Zhong Wang[a,b+], Xiaoyu Zhang[a], Hui Wang[a]

[a] *Key Laboratory of Industrial Ecology and Environmental Engineering, School of Environmental Sciences and Technology, Dalian University of Technology, Dalian, 116024, China*

[b] *Key Laboratory of Biofuels, Qingdao Institute of Bioenergy and Bioprocess Technology, Chinese Academy of Sciences, Qingdao, 266101, China*

Abstract

Novel Cu-Ce-Zr mixed oxides were synthesized by citric acid sol-gel methods, and it exhibited an excellent NH_3-SCO activity (180°C, TOF=1.33 h^{-1}). The finely dispersed CuO, Cu-Ce-Zr solid solution and monomeric Cu^{2+} ions in octahedral sites were the main active sites. The finely dispersed CuO species was NH_3 adsorption sites, and this adsorption capacity could be improved by its good reducibility. The Cu-Ce-Zr solid solution was an important intermediate in oxygen transfer from bulk to surface. *In-situ* EPR analysis indicated that the isolated Cu^{2+} locating in octahedral sites was more active compared with that of locating in square-planar pyramidal sites, and it induced the formation of more Cu-Ce-Zr solid solution. Meanwhile, *in-situ* O_2-TPD result showed that both adsorbed oxygen and bulk lattice oxygen were active oxygen adspecies, and the adsorbed oxygen were more active than bulk lattice oxygen

[+] These authors contributed equally to this work

* To whom correspondence should be addressed. E-mail: quzhenping@dlut.edu.cn. Tel/Fax: 0086-411-84708083

in NH_3 oxidation.

Keywords: Cu-Ce-Zr; Octahedral sites; Preparation method; Selective catalytic oxidation of ammonia

1 Introduction

The selective catalytic oxidation (SCO) of NH_3 to nitrogen was one of effective technology for abating NH_3 and consequently it has become of increasing interest in recent years [1, 2]. The metal oxide catalyst with low cost has been demonstrated to be one of the most efficient catalysts for the NH_3-SCO reaction. Up to now, CuO/La_2O_3 [3], M-Mg-Al (M=Ni, Fe, Cu and Co) [4], Mg-Cu-Fe [5], CuO/RuO_2 [6] and Cu-Ce [7] metal oxide catalysts have been developed. Our previous study found that the Ce-Zr mixed oxides showed the NH_3 oxidation activity to a certain extent and higher N_2 selectivity [8]. Recently, Yan et al. [9] demonstrated that the modifying with Ru for $Ce_{0.6}Zr_{0.4}O_2$ could facilitate NH_3 oxidation, though the operation temperature was still quite high (> 350^{o}C). Afterward, the $CuO\text{-}CeO_2$ catalyst prepared by surfactant-templated method exhibited a high molar ratio of finely dispersed CuO species and strong synergetic interaction between copper oxide species and cerium oxides, which significantly decreased the operation temperature ($\sim$250^{o}C) [10]. Unfortunately, the thermal resistance of $CuO\text{-}CeO_2$ mixed oxides need to be further enhanced. In addition, in spite of all the studies reporting the different factors that influenced redox properties and catalytic behavior of Cu catalyst, the nature of the active sites has not been

completely elucidated. Some authors [11] indicated that the catalytic activity was correlated with the concentration of isolated Cu^{2+} in a square planar coordination, while others have shown that well dispersed CuO species exhibited much higher activity and reducibility compared to the exchanged Cu ions [12]. Thus the coordination environment and the roles of Cu species need to be further confirmed.

Recently, a large number of works have been focused on the ternary mixed oxides for various catalytic reactions. Most researchers believed that the synergistic interaction of different components increased the dispersion degree of active constituents, and its several properties such as reducibility, pore structure, and mechanical and chemical properties could be also obviously improved, which finally determined their excellent catalytic activities and stabilities [13-15]. It has been known that the preparation method was a better way to adjust the dispersion of the active component. Compared with MnO_x/TiO_2 prepared by an impregnation or co-precipitation method, the catalyst prepared by sol-gel method exhibited a fine dispersion of manganese oxides and higher activity and better tolerance to SO_2 in NH_3-SCR [16]. Moreover, varying preparation method often led to the change in coordination environment and location of metal ions and metal oxide in catalyst [17]. Especially, for metal-modified CeO_2 catalysts, the more labile oxygen and enhanced oxygen storage capacity were also obtained when there was a truly homogenous distribution of metal ions [18].

In the present study, the dispersion of active components, reducibility of metal oxides, the concentration of oxygen vacancies and the mobility of lattice oxygen over

Cu-Ce-Zr mixed oxides were well adjusted by optimizing the preparation methods. The novel ternary Cu-Ce-Zr catalyst prepared by citric acid sol-gel method showed the excellent activity for NH_3 oxidation ($T_{90\%}$=190^{o}C). The role of different coordination environment and location of Cu species were systematically studied by *in situ* EPR, and the active oxygen species was also confirmed by *in situ* O_2-TPD.

2 Experimental

2.1 Catalyst preparation

The ternary metal oxides catalysts were prepared by citric acid sol-gel method (SOL), homogeneous precipitation method (HP), incipient wetness impregnation method (IW), respectively. In all samples, the molar ratio of Ce/Zr was 4, and the Cu loading content was 6 wt%. All samples were calcined at 450^{o}C for 3 h in air. The detailed procedures are described in the Supporting Information. The as-prepared samples were referred to Cu-Ce-Zr (SOL), Cu-Ce-Zr (HP), Cu/Ce-Zr (IW), Cu/CeO_2-ZrO_2 (IW).

2.2 Catalyst characterization

XRD experiment was recorded on a Rigaku D/max-γb X-ray diffractometer with monochromatic detector equipped with CuKα radiation. The bulk metal composition was determined by inductively coupled plasma atomic emission spectrometry (ICP-AES, OPTIMA 2000). XPS was measured using an X-ray photoelectron spectrometer (ESCALAB 250Xi, Thermo) with a monochromatic X-ray source of Al

Kα under ultra-high vacuum (3~2×10^{-6} Pa). H_2-TPR was performed on a Chem BET TPR/TPD Chemisorptions Analyzer. The NH_3-TPD were performed in a fixed-bed reaction using quadrupole mass spectrometer (GSD 320). O_2-TPD was also performed by quadrupole mass spectrometer (GSD 320) on a fixed-bed continuous flow micro-reactor system. *In-situ* electron paramagnetic resonance (EPR) measurements were performed at room temperature using a Bruker (A200-9.5/12) operating at the X band (~9.8 GHz).

2.3 Catalytic activity tests

The NH_3-SCO activity was studied in a fixed-bed flow reactor (8 mm in interior diameter) using 200 mg of catalyst. The typical reactant gas composition was as follows: 1000 ppm NH_3, 10 vol% O_2, and balance He. The total flow rate of the reaction mixture was 100 ml/min, and the gas hourly space velocity (GHSV) was about 40000 h^{-1}. The inlet and outlet gas were analyzed by Gas Chromatograph using a 5A column with a TCD detector for N_2 and the NH_3 analyzer (GXH-1050, Beijing) to monitor the concentration of ammonia.

Turnover Frequency (TOF) is defined as the number of NH_3 molecules converted per surface active Cu site per second.

$$\mathrm{TOFs} = \frac{C_{\mathrm{NH_3}} X_{\mathrm{NH_3}} V_{\mathrm{gas}} M_{\mathrm{Cu}}}{m_{\mathrm{cat}} w_{\mathrm{Cu}} D_{\mathrm{Cu}}} \ [\mathrm{h^{-1}}]$$

where C_{NH_3} is the concentration of NH_3; X_{NH_3}, the conversion of NH_3 based on N_2 formation within the differential kinetic regime (NH_3 conversion below ~10%); V_{gas}, the total molar flow rate; M_{Cu}, the atomic weight of Cu; m_{cat}, the mass of

catalyst in the reactor bed; w_{Cu}, the mass fraction of Cu measured by ICP; D_{Cu}, the dispersion of Cu determined by N_2O oxidation and followed H_2 titration using the procedure described by Van Der Grift et al. [19].

3 Results

3.1 Distribution of Cu species in catalysts

Fig. 1 shows the XRD patterns of different catalysts. The strong diffraction peaks of cubic fluorite-phase CeO_2 were observed at $2\theta=28.5^o$, 33.3^o, 47.7^o, and 56.8^o, corresponding to the (111), (200), (220), and (311) crystal faces over pure CeO_2 catalyst [20]. It was interesting to note that the diffraction peaks shifted to higher angles with the co-incorporation of both Cu and Zr. And no peaks splitting for the three phases (Cu, Ce and Zr) were detected, which suggested the formation of Cu-Ce-Zr solid solution [21]. In addition, for the Cu/Ce-Zr (IW) catalyst, the small diffraction peaks for bulk CuO ($2\theta=35.4^o$ and 38.5^o) could be identified [22]. No CuO characteristic diffraction peaks were observed for other three samples, and the copper species were in the form of Cu-Ce-Zr solid solution or a combination of the finely dispersed CuO and Cu-Ce-Zr solid solution.

H_2-TPR behaviors was used to confirm the state of Cu species, as shown in **Fig. 2A**. Generally, the reduction of Zr^{4+} occurred above 1000^oC and the Ce^{4+} for surface and bulk ceria could be reduced at least 500^oC and 780^oC [23, 24], respectively. Thus the reduction peaks in the range of $100\text{-}500^oC$ were attributed to the reduction of Cu species for all mixed oxides. The zone (I) peaks were proposed as the reduction of the

finely dispersed CuO species strongly interacting with ceria, whereas the zone (II) peaks were due to the reduction of Cu^{2+} ions in Cu-Ce-Zr solid solution [10, 25]. The zone (III) peaks were related to the reduction of bulk CuO [26]. Combining with XRD results, it was reasonable to conclude that finely dispersed CuO species and Cu-Ce-Zr solid solution existed in all samples. And the bulk CuO species was only observed in Cu/CeO_2-ZrO_2 (IW) and Cu/Ce-Zr (IW) catalysts. The incipient wetness impregnation method decreased the homogeneity of mixed oxides compared with single step method, resulting in the formation of bulk CuO. Moreover, it was found that more bulk CuO was formed on the Cu/Ce-Zr (IW) sample.

Meanwhile, EPR technology was used to probe the hyperfine structure of Cu species, as shown in **Fig. 3**. By analyzing the hyperfine features of catalysts, a doublet spectral features centered at $g_{\perp}$=2.060 ($A_{\perp}$=14 G) (labeled K) appeared, which has been reported to be resulted from the Cu^{2+} dimers [27]. Usually, the shortest separation distance between neighboring Ce^{4+} ions was 3.811Å in the lattice. Then it was possible that such Cu^{2+} ions (3.5Å) was located by substitution of two Ce^{4+} in neighboring positions, so the type K signal could be observed. This also provided the predominant evidence for the formation of Cu-Ce-Zr solid solution, which was in agreement with the XRD and H_2-TPR results. Another broad and poorly resolved signal B centered around at g=2.130 was observed over all samples. Its wide line shape and unresolved hyperfine splitting might be attributed to the dipolar broadening effects produced by mutual interactions between paramagnetic Cu^{2+} ions, suggesting that the corresponding ions were located in a Cu^{2+}-containing aggregated phase or Cu

oxide clusters [28]. Thus the finely dispersed CuO species should be responsible for the B signal. In addition, two A signals (A_1 and A_2) corresponding to the isolated monomeric Cu^{2+} ions in sites with an axial symmetry environment were observed. A central signal (A_1) around at $g_{//}$=2.211 ($A_{//}$=170 G) and $g_{\perp}$=2.054 ($A_{\perp}$=28 G) composed of four narrow hyperfine splitting in its parallel and perpendicular components, which was attributed to Cu^{2+} ions in octahedral sites with tetragonal distortion [29]. The signal A_2 with well-resolved hyperfine structure at least in parallel component ($g_{//}$=2.152, $A_{//}$=81 G) was correlated with Cu^{2+} species in square-planar pyramidal sites [30]. The EPR results not only provided an additional evidence for the formation of finely dispersed CuO and Cu-Ce-Zr solid solution, but also confirmed the existence of isolated monomeric Cu^{2+} ions in octahedral or square-planar pyramidal sites.

3.2 Oxygen species in catalysts

The catalysts were further investigated by XPS to examine the surface chemical state, and the results are shown in **Fig. 4**. The peaks marked as *u*, *u"* and *u"'* were attributed to Ce^{4+} $3d_{3/2}$, and those labeled as *v*, *v"*, *v"'* were arising from Ce^{4+} $3d_{5/2}$ [31]. Compared with the bands of Ce^{4+} 3d, the bands *u'* and *v'* corresponded to the Ce^{3+} $3d_{3/2}$ and Ce^{3+} $3d_{5/2}$ contributions, respectively [32]. These results indicated that Ce was in a partially reduced state on the surfaces, which might be attributable to the interaction between Cu and Ce. In addition, the presence of Ce^{3+} resulted in a charge imbalance, and leaded to the formation of oxygen vacancies [33]. Yet, in the Cu 2p XPS

spectra (**Fig. 4B**), the shake-up peak and Cu $2p_{3/2}$ (933.6 eV) as well as Cu $2p_{1/2}$ (953.5 eV) peaks were observed, which were characteristic of Cu^{2+} [34]. However, the lower Cu $2p_{3/2}$ binding energy (931.2 eV) and the absence of the shake-up peak were characteristic of Cu^{+} [35]. That was to say, it was apparent that the Cu^{2+} and Cu^{+} was coexistence in original samples. Thus, it was probably suggested that the transient generation of oxygen vacancy for fresh samples during calcination followed this process:

$$2Ce^{4+}\text{-}OH+2Cu^{2+}\text{-}OH \xrightarrow{-2H_2O} Ce^{3+}\text{-}\blacksquare\text{-}Cu^{+}+O^{-}\text{-}Ce^{4+}\text{-}Cu^{2+}\text{-}O^{-} \quad (1)$$

Usually, oxygen molecules were easily adsorbed at the oxygen vacancies of an oxide material [36]. As shown in **Fig. 4C,** the asymmetrical O 1s signal could be deconvoluted to two components. The broad shoulder at a higher BE (531.2 eV) was assigned to the surface adsorbed oxygen species (O_{ads}), whereas the peak at ～529.1 eV was attributed to the surface lattice O^{2-} (O_{latt}) [37]. The instantaneous formation of O_{ads} by adsorbing O_2 at oxygen vacancy during calcination followed this step:

$$Ce^{3+}\text{-}\blacksquare\text{-}Cu^{+}+2O_2 \rightarrow O_2^{-}\text{-}Cu^{2+}\text{-}Ce^{4+}\text{-}O_2^{-} \quad (2)$$

This phenomenon was also implying the existence of oxygen vacancies in catalysts. The O_2-TPD profiles directly exhibited the O_2 desorption behavior in catalysts, and the results are shown in **Fig. 5**. Three distinct peaks centered at 485-610°C, 715-750°C and 770-860°C were observed. Generally speaking, the signals recorded below 700°C could be ascribed to the α-O_2 desorption and originated from the oxygen species adsorbed on the surface oxygen vacancies [38], coinciding with the result of XPS (**Fig. 4C**). According to Eq. (1) and Eq. (2), the α-O_2 desorption was proposed

195 by the following two reactions process:

$$O^{-}\text{-}Ce^{4+}\text{-}Cu^{2+}\text{-}O^{-}+O_2^{-}\text{-}Ce^{4+}\text{-}Cu^{2+}\text{-}O_2^{-}\rightarrow 2Ce^{4+}\text{-}O^{2-}\text{-}Cu^{2+}+2O_2 \quad (3)$$

$$O_2^{-}\text{-}Ce^{4+}\text{-}Cu^{2+}\text{-}O_2^{-}\rightarrow Ce^{3+}\text{-}\blacksquare\text{-}Cu^{+}+2O_2 \quad (4)$$

196 It was obvious that the α-O_2 desorption was directly related to the oxygen species
197 adsorbed on the oxygen vacancy, so the amount of α-O_2 species could be considered
198 as a measure of the density of oxygen vacancies. Whereas those recorded above
199 700^{o}C were known as β-O_2 desorption, and two distinct β-O_2 peaks centered at β_1-O_2
200 (715-750^{o}C) and β_2-O_2 (770-860^{o}C) were liberated from the surface and bulk lattice
201 leaving oxygen vacancies and the reduced cations, respectively [39]. This β_1-O_2 peak
202 appeared in O_2-TPD patterns through this step:

$$\underset{\text{surface}}{Ce^{4+}\text{-}O^{2-}\text{-}Cu^{2+}}\rightarrow\underset{\text{surface}}{Ce^{3+}\text{-}\blacksquare\text{-}Cu^{+}}+\frac{1}{2}O_2 \quad (5)$$

203 The bulk β_2-O_2 desorption firstly proceeded via the diffusion of oxygen from bulk to
204 surface (Eq. (6)).

$$\underset{\text{bulk}}{Ce^{4+}\text{-}O^{2-}\text{-}Cu^{2+}}+\underset{\text{surface}}{Ce^{3+}\text{-}\blacksquare\text{-}Cu^{+}}\rightarrow\underset{\text{surface}}{Ce^{4+}\text{-}O^{2-}\text{-}Cu^{2+}}+\underset{\text{bulk}}{Ce^{3+}\text{-}\blacksquare\text{-}Cu^{+}} \quad (6)$$

205 Thereafter, β_2-O_2 desorption in O_2-TPD proceeded through Eq. (5). The O_2 desorption
206 behavior also indeed indicated that the evolution of oxygen vacancies was related to
207 formation of Cu-Ce-Zr solid solution. Meanwhile, lattice oxygen mobility could be
208 reflected by the amount as well as the onset temperature of β-O_2 desorption.

209 **3.3 Catalytic performance of catalysts for NH_3 oxidation**

210 **Fig. 6** shows the catalytic performance of the catalysts prepared by different
211 methods for NH_3 oxidation. In all cases, the N_2 selectivity was above 90% (**Fig. 6B**).

Cu-Ce-Zr (SOL) catalyst demonstrated the highest activity. $T_{50\%}$ and $T_{90\%}$ (the reaction temperatures of 50% and 90% NH_3 conversion) are listed in **Table 1**. Apparently, the Cu-Ce-Zr (SOL) catalyst showed the lowest $T_{50\%}$ (160°C) and $T_{90\%}$ (190°C). The $T_{90\%}$ of Cu-Ce-Zr (HP), Cu/CeO_2-ZrO_2 (IW) and Cu/Ce-Zr (IW) increased by 40, 70 and 100°C than Cu-Ce-Zr (SOL), respectively. In order to verify the TOF was in the kinetic regime and not affected by heat and mass transport limitations, the Madon-Boudart test of Cu-Ce-Zr (SOL), which was an effective verification method, was carried out in **Fig. S1-S2.** All slopes from plots of ln r vs. ln f_m were about unity, suggesting the absence of any heat and mass transfer limitations in NH_3-SCO over Cu-Ce-Zr catalysts. From **Table 1** and **Fig. 7**, it was found that the TOF order at 180°C was Cu-Ce-Zr (SOL) (1.33 h^{-1}) > Cu-Ce-Zr (HP) (1.03 h^{-1}) > Cu/CeO_2-ZrO_2 (IW) (0.85 h^{-1}) > Cu/Ce-Zr (IW) (0.72 h^{-1}). Among these catalysts, Cu-Ce-Zr (SOL) catalyst demonstrated the highest TOF value, which suggested that Cu-Ce-Zr (SOL) catalyst contained the largest amount of active Cu species of the per unit mass in NH_3 oxidation reaction.

Table 2 shows the catalytic performance of different catalysts in NH_3 oxidation. It could be seen that except for CuO/RuO_2 catalyst with a high amount of RuO_2 [6], the catalytic performance of Cu-Ce-Zr (SOL) catalyst was superior to that of other Cu catalysts, especially for NH_3 conversion [10, 40, 41]. Compared with other transition metal catalysts, the Cu-Ce-Zr (SOL) always exhibited perfect NH_3 conversion and N_2 selectivity [42-44]. The $T_{100\%}$ of Cu-Ce-Zr (SOL) catalyst was even lower 280°C than that of MoO_3/SiO_2 catalyst. Moreover, the TOF of Cu-Ce-Zr (SOL) catalyst (1.33 h^{-1},

180°C) was larger than that of Mn/SiO_2 catalyst (1.01 h^{-1}, 230°C) [43]. The Cu-Ce-Zr (SOL) catalyst was more active in transition metal catalysts. For noble metal catalysts, CuO/RuO_2 and Ir/Al_2O_3 catalyst showed the lower $T_{100\%}$ than Cu-Ce-Zr (SOL) catalyst [45]. The $T_{100\%}$ of Au/Al_2O_3 was 380°C, which was higher than that of Cu-Ce-Zr (SOL) catalyst [46]. However, the N_2 selectivity of Pt-ZSM-5 and Ir/Al_2O_3 catalysts was poor [45, 47]. Therefore, the Cu-Ce-Zr (SOL) catalyst was a very potential catalyst for NH_3 oxidation.

3.4 The resistance to SO_2, H_2O and CO_2 poisoning as well as thermal stability of Cu-Ce-Zr (SOL)

In industrial application, the resistances to SO_2, H_2O and CO_2 poisoning as well as the thermal stability were very important. So the correlation studies were carried out over Cu-Ce-Zr (SOL) catalyst at 220°C, and these results are shown in **Fig. 8**. It was noticeable that the presence of 5% H_2O slightly decreased the NH_3 conversion due to the competitive adsorption of H_2O with NH_3 on the same active sites [48]. The presence of 100 ppm SO_2 inhibited the NH_3-SCO reaction, and the NH_3 conversion decreased to about 94%, which was probably ascribed to the sulfation of active phase and deposition of ammonium sulfate [49]. The coexistence of SO_2 and H_2O implied the synergistic inhibit effect on the NH_3-SCO performance, and approximate 92% of NH_3 conversion was obtained, which was probably due to the enhanced degree of sulfation for Cu-Ce-Zr (SOL) catalyst [50]. Upon switching off the H_2O or SO_2, respectively, the activity was rapidly restored to above 97% of its original level. However, when 5%

CO_2 was added, the NH_3 conversion decreased significantly to ~81%. Upon removal of the CO_2 supply, only ~90% NH_3 conversion was gradually restored. In addition, the TOF in the presence of SO_2, H_2O and CO_2 was calculated from the conversion plots using only data in the kinetic region at 180°C, as shown in **Fig S3**. Note that the TOF in presence of H_2O, SO_2, SO_2 + H_2O and CO_2 was 1.25, 1.17, 1.09, 0.81 h^{-1}, respectively. The presence of CO_2 induced a significant decrease of TOF. And it was found that the NH_3 conversion was still higher than 93% at 220°C after hydrothermal treatment over fresh Cu-Ce-Zr (SOL) at 800°C for 24 h. The above results suggested that Cu-Ce-Zr (SOL) catalyst exhibited the excellent SO_2/H_2O poisoning resistance and hydrothermal stability.

4 Discussion

In NH_3 oxidation, several factors were associated with the catalytic activity. The catalytic activity was thought to be related to be reducibility and dispersion of active phase for NH_3 oxidation. Amblard et al. [51] have proposed that the Mn/Al_2O_3 and Fe/Al_2O_3 were more active than Ni/Al_2O_3 for NH_3 oxidation, possibly because of the enhanced redox properties. The presence of small Co_3O_4 crystallites in the silica-supported Co_3O_4 catalyst resulted in a higher effective utilization of cobalt in NH_3 oxidation mainly due to the higher dispersion [52]. Gang et al. [45] also suggested the higher activity of NH_3 oxidation was probably due to the small particle size and better dispersion of copper oxide on the support. Importantly, ammonia oxidation activity at low temperatures was also related to the dissociative or non-dissociative adsorption

ability of oxygen on the catalyst [53, 54]. According to the results reported by Long et al. [55], the variable valence of Cu^{+}/Cu^{2+} in Cu-ZSM-5 catalyst might be beneficial to oxygen adsorption and activation, therefore, a high activity for the NH_3-SCO reaction was expected. According to the above investigated results, the promotional effect aspects in NH_3-SCO over Cu-Ce-Zr catalysts were further discussed in the following.

In our research, the H_2-TPR analysis (**Fig. 2B)** indicated that the relative content of finely dispersed CuO on catalysts was varied in the order of Cu-Ce-Zr (SOL) > Cu-Ce-Zr (HP) > Cu/CeO_2-ZrO_2 (IW) > Cu/Ce-Zr (IW), and the reduction temperature of CuO species shared the opposite sequence. Usually, the higher the dispersion was, the lower the reduction temperature of CuO species [56]. The surface Cu/Ce atomic ratio estimated by XPS (**Fig. 4**) is presented in **Table 3**. Compared with the bulk compositions of all samples, it could be observed that the surface Cu/Ce atomic ratio was more than three times higher, indicating a significant enrichment of the surface highly dispersed CuO species. The surface Cu/Ce atomic ratio was varied in the order of Cu-Ce-Zr (SOL) > Cu-Ce-Zr (HP) > Cu/CeO2-ZrO_2 (IW) > Cu/Ce-Zr (IW), whose result was in agreement with the H_2-TPR analysis result **(Fig. 2B**). Moreover, the EPR results in **Fig. 3B** also showed the gradual decrease of B signal intensity from (a) to (d) catalysts, which suggested the amount decrease of finely dispersed CuO species in different catalysts. Combining with the TOF results (**Fig. 7 and Table 1**), the order of TOF was consistent with the varieties of finely dispersed CuO, and the higher dispersion of CuO species induced the higher TOF value. Thus, the finely dispersed CuO species in catalysts was an important reason for the

enhanced NH_3-SCO activity. Meanwhile, the lower TOF in Cu/CeO_2-ZrO_2 (IW) and Cu/Ce-Zr (IW) catalysts should be related with the formation of bulk CuO species revealed by XRD and H_2-TPR. Generally, reducibility was also an important factor influencing the catalytic activity of a material [57]. **Fig. 2B** shows the quantitative analysis result of H_2-TPR. The temperature of reduction peak (T_{red}) was taken as a measure to evaluate the redox ability of catalyst. It was known that the lower was the temperature of reduction peaks (T_{red}), the stronger was the redox ability of catalyst [58]. It was observed that T_{red} for all copper species increased in sequence of Cu-Ce-Zr (SOL) < Cu-Ce-Zr (HP) < Cu/CeO_2-ZrO_2 (IW) < Cu/Ce-Zr (IW). The Cu-Ce-Zr (SOL) catalyst with the best reducibility led to the excellently high catalytic performance.

To achieve deeper insight into the role of finely dispersed CuO species, the NH_3-TPD experiment was carried out (**Fig. 9**). Two peaks of ammonia desorption appeared, indicating that two major ammonia species with different thermal stability existed on the catalyst surface. The lower temperature peak (155^{o}C) should be attributable to the physically adsorbed NH_3, while the higher temperature peak (230^{o}C) should correspond to the chemisorbed NH_3 [44]. The relative desorption amount of NH_3 was calculated by the fitting area of NH_3 desorption peak (**Table 3**). It was observed that the total desorption amount, especially the desoprtion amount of chemisorbed NH_3, were ranked as follows: Cu-Ce-Zr (SOL) > Cu-Ce-Zr (HP) > Cu/CeO_2-ZrO_2 (IW) > Cu/Ce-Zr (IW). This was in parallel with the amount of the highly dispersed CuO species (**Fig. 2B**). The formation of finely dispersed CuO species was suggested

to be in favor of the adsorption of NH_3, which could significantly improve in the NH_3 adsorption capacity and TOF for NH_3 oxidation.

In order to investigate the transition of different active phase during NH_3 oxidation process, the *in-situ* EPR spectrum of Cu-Ce-Zr (SOL) catalyst under different reaction conditions are shown in **Fig. 10**. The addition of NH_3 flow at room temperature on Cu-Ce-Zr (SOL) sample (**Fig. 10b**) did not cause any change in the intensity or shape of the EPR spectrum (A_1, A_2, B and K signals). In contrast, up to 230^{o}C in a flow of He on original Cu-Ce-Zr (SOL) sample, all signal intensity and the hyperfine structure (**Fig. 10c**) increased compared with that of original spectrum (**Fig. 10a**), which should be related to the impurities removal after high temperatures treatment. When the original Cu-Ce-Zr (SOL) catalyst was carried out under a flow of NH_3 instead of He at 230^{o}C (**Fig. 10d**), an important increase in the B signal was observed compared with EPR spectrum of Cu-Ce-Zr (SOL) sample treated by He at 230^{o}C (**Fig. 10c**). It was known that the intensity of B signal was correlated with the highly dispersed copper oxide on the surface [59]. Particularly, the higher was the dispersion of CuO species, the larger fraction of copper oxide was detected by EPR. The H_2-TPR result (**Fig. S4**) showed that the reduction temperature of finely dispersed CuO over Cu-Ce-Zr (SOL) treated in NH_3 at 230^{o}C shifted toward lower temperature, and the amount was also increased. Thus, NH_3 atmosphere could promote the dispersion of finely dispersed CuO in the catalyst during NH_3 oxidation. However, when the Cu-Ce-Zr (SOL) sample treated by NH_3 at 230^{o}C was re-oxidized (**Fig. 10e**), the A_2 signal remained stable and the decrease of A_1 and B signals

intensities was recorded compared with EPR spectrum of Cu-Ce-Zr (SOL) sample treated by NH_3 at 230^{o}C (**Fig. 10d**). However, the intensity of K signal was observed to be significantly increased. In order to clarify the evolution of Cu species in re-oxidized Cu-Ce-Zr (SOL) catalyst, the H_2-TPR experiment was also carried out (**Fig. S4**). It was observed that the reduction temperature of finely dispersed CuO species shifted to higher temperature, so the lower dispersion of CuO species induced the decrease of B signal intensity. It was known that the Cu^{2+} ions (A_1) was surrounded by fewer oxygen anions than Cu^{2+} ions (A_2), the difference in the coordination number determined that the Cu^{2+} ions corresponding to the A_1 signal were more accessible towards the oxygen than that corresponding to the A_2 signal [59]. In addition, the Cu^{2+} ion monomers (A_1) was the precursor of the dimmer (K) due to the similar g value for the two signals and the double hyperfine splitting constants of A_1 compared with K signal [60, 61]. So the monomeric Cu^{2+} ions of A_1 signal were more accessible to combine with O_2 to form copper (II) ions dimers, which could induce a migration of Cu^{2+} ions from their sites (A_1 signal) to copper (II) ions dimers (K signal). So the increase of K signal and the decrease of A_1 signal intensities were observed in **Fig. 10e.** As shown in **Fig. 3B**, the A_1 signal became very weak and unresolved from Cu-Ce-Zr (SOL) to Cu-Ce-Zr (HP) catalyst, and then disappeared for Cu/CeO_2-ZrO_2 (IW) and Cu/Ce-Zr (IW) catalysts. The variation of A_1 signal in different catalysts also paralleled the reaction TOF. However, the A_2 signal always appeared for all catalysts. Thus, the isolated Cu^{2+} locating in octahedral sites with tetragonal distortion (A_1) was more active compared with that of locating in

square-planar pyramidal sites, and it induced the more formation of Cu-Ce-Zr solid solution. Apparently, Cu-Ce-Zr (SOL) catalysts showed the strongest K signal (Cu-Ce-Zr) in **Fig. 3B**, and the K signal became unobvious in the spectrum of Cu-Ce-Zr (HP) and almost absent in the case of other catalysts. Furthermore, combining with the reaction TOF (**Fig. 7**) and the O_2 desorption behavior (**Fig. 5**), it would indicate that the Cu-Ce-Zr solid solution was the important supporter of oxygen transfer. More importantly, when the Cu-Ce-Zr (SOL) sample re-oxidized by 230^{o}C (**Fig. 10e**) was re-treated again by NH_3 at 230^{o}C (**Fig. 10f**), the evolution of K, A_1 and B signal intensities was opposite of the result in **Fig. 10e**. Similarly, the increase in the B signal intensity should be attributed to the higher dispersion of CuO in the role of NH_3. Since the NH_3 could be mainly adsorbed on the surface of finely dispersed CuO, the decrease of K signal intensity should be due to the reaction of the adsorbed NH_3 with active oxygen species in Cu-Ce-Zr solid solution (K). Meanwhile the K signal was transformed into the A_1 signal, and more Cu^{2+} ions in octahedral sites with tetragonal distortion (A_1 signal) was formed (**Fig. 10f**). It was further defined that finely dispersed CuO, monomeric Cu^{2+} ions locating in octahedral sites (A_1) and Cu-Ce-Zr solid solution were active sites in NH_3 oxidation reaction.

Meanwhile, it seemed that oxygen species was responsible for the coupling of the two Cu^{2+} (A_1 signal) making up the dimer (Cu-Ce-Zr solid solution) in NH_3 oxidation reaction. Yet, the relatively total amount of oxygen adspecies followed the orders of Cu-Ce-Zr (SOL) (1.00) > Cu-Ce-Zr (HP) (0.91) > Cu/CeO_2-ZrO_2 (IW) (0.86) > Cu/Ce-Zr (IW) (0.57) (**Table 3**), which was also in accordance with the TOF

value. Therefore, the following section was required to analyze the role of oxygen during NH_3-SCO reaction.

The substitution of Cu and Zr for Ce generated an electronic unbalance, and as a consequence, the oxygen vacancies could be produced to preserve the charge neutrality. The transient generation of oxygen vacancy for fresh samples from Eq. (1) indicated that the relative surface content of Ce^{3+} also reflected the amount of oxygen vacancies. Moreover, the O_{ads} (α-O_2) species were adsorbed at oxygen vacancies. Thus, on the basis of the surface content of Ce^{3+} and O_{ads}/O_{latt} values (**Table 3**), one could see that the concentration of oxygen vacancies decreased in the order Cu-Ce-Zr (SOL) > Cu-Ce-Zr (HP) > Cu/CeO_2-ZrO_2 (IW) > Cu/Ce-Zr (IW), coinciding with the reaction TOF (**Fig. 7**). That was to say, the oxygen vacancies was a significant factor to sustain the higher reaction TOF.

Apart from α-O_2 species, the reaction TOF was also often discussed in terms of the mobility and activated ability of lattice oxygen (β-O_2). Usually, the β-O_2 species was related to the reducibility of metal ions [62]. The above analysis indicated that the Cu-Ce-Zr solid solution was the important supporter of β-O_2. By comparing the reducibility of Cu-Ce-Zr solid solution (**Fig. 2**), it was found that this reducibility decreased according to the sequence of Cu-Ce-Zr (SOL) > Cu-Ce-Zr (HP) > Cu/CeO_2-ZrO_2 (IW) > Cu/Ce-Zr (IW). The result agreed well with the amount of β-O_2 species and was inconsistent with the desorption temperature of β-O_2 species **(Table 3**). It could be realized that the easier reduction of Cu-Ce-Zr solid solution induced the strong mobility and activated ability of lattice oxygen (β-O_2) **(Fig. 5)**, finally led

to the higher TOF (**Fig. 7**). Thus, the lattice oxygen species played an important role under reaction conditions, especially for the Cu-Ce-Zr (SOL) catalyst. In order to clarify the role of oxygen species in NH_3 oxidation, the effect of O_2 concentration on the catalytic performance over Cu-Ce-Zr (SOL) sample was also studied in this work, as shown in **Fig. 11A.** With the increase of O_2 concentration from 1 to 4 vol.% in the reactants, the NH_3 conversion showed the monotonic increase at 220^{o}C. When O_2 concentration reached above 4 vol.%, the NH_3 conversion did not show monotonic increase at 220^{o}C. This indicated that the O_2 molecule and adsorbed oxygen species achieved a balanced state at this value (4 vol.%). Interestingly, the NH_3 conversion only declined to 90% when 4 vol.% O_2 was cut off (**inset in Fig. 11A**). And then, it took a long time (nearly 3 h) to decrease from 90 to 26%. When the O_2 molecular was introduced into the reactants again, and an immediate rebound of NH_3 conversion to 100% was observed. In order to clarify the variation of oxygen species in this process (**inset in Fig. 11A**), the *in-situ* O_2-TPD experiment was also carried out for the Cu-Ce-Zr (SOL) at the point of O_2-A, O_2-B, O_2-C and O_2-D in **Fig. 11B**. Compared with the original Cu-Ce-Zr (SOL) catalyst (**Fig. 5a**), a clear shift of α-O_2 species toward lower temperature was observed in the profile of O_2-A (**Fig. 11B**), however, the desorption of β_1-O_2 species was not observed. This phenomenon suggested that the adsorbed oxygen species than bulk lattice oxygen were more important in oxygen cycles. However the α-O_2 species disappeared in the pattern of O_2-B. Meanwhile, the desorption peak of β_2-O_2 also shifted to higher temperatures, which should be related to the deactivation of oxygen mobility when α-O_2 species disapperared. After this, the

β_2-O_2 species in the pattern of O_2-C significantly decreased compared with that of O_2-B. When 4 vol.% O_2 was added into the stream again, the α-O_2 and β_2-O_2 species sharply increased in the pattern of O_2-D. From the above analysis, it was concluded that the α-O_2 species could be quickly consumed when O_2 was cut off, which induced the NH_3 conversion sharply dropped to 90%. In the subsequent process, the β_2-O_2 species gradually reacted with NH_3 and the NH_3 conversion finally decreased to 26%, indicating that the adsorbed oxygen species could result in the higher NH_3 oxidation activity than bulk lattice oxygen. When O_2 was re-added to the reactants, the oxygen cycle was recovered in NH_3-SCO reaction.

As stated above, **Fig. 12** shows the reaction models of NH_3 oxidation on Cu-Ce-Zr (SOL) catalyst. The NH_3 was mainly adsorbed on the surface of finely dispersed CuO species. In the absence of gaseous O_2, the surface adsorbed O_2 in Cu-Ce-Zr solid solution could be reacted with adsorbed NH_3, and meanwhile the oxygen vacancies was formed in Cu-Ce-Zr solid solution. When the surface adsorbed O_2 was consumed, the lattice oxygen constantly transferred from bulk to surface in Cu-Ce-Zr solid solution, which was involved in the NH_3 oxidation. Moreover, it seems that the adsorbed oxygen species were more active than bulk lattice oxygen species. In the presence of gaseous O_2, compared with monomeric Cu^{2+} in square-planar pyramidal sites, the Cu^{2+} ions in octahedral sites were more accessible towards the oxygen to form Cu-Ce-Zr solid solution in NH_3 oxidation. Meanwhile, the surface oxygen vacancies was readily replenished by gaseous O_2 with regeneration of surface active oxygen, which would promote the adsorption and

454 dissociation of oxygen molecule and facilitate the NH_3 oxidation reaction.

455

456 **5 Conclusions**

457 The Cu-Ce-Zr catalyst prepared by citric acid sol-gel method (SOL) exhibited
458 the best catalytic activity ($T_{90\%}$=190^{o}C). The excellent activity could be attributed to
459 the finely dispersed CuO, Cu-Ce-Zr solid solution and monomeric Cu^{2+} ions in
460 octahedral sites. During the NH_3-SCO reaction, the finely dispersed CuO species
461 acted as the crucial adsorption sites of NH_3, meanwhile, the NH_3 also favored the
462 dispersion of CuO species. The Cu-Ce-Zr solid solution was an important
463 intermediate in oxygen transfer from bulk to surface in NH_3 oxidation. Compared
464 with monomeric Cu^{2+} in square-planar pyramidal sites, the Cu^{2+} ions in octahedral
465 sites were more accessible towards the oxygen to form Cu-Ce-Zr solid solution.
466 Meanwhile, *in situ* O_2-TPD result showed that both adsorbed oxygen and bulk lattice
467 oxygen were active oxygen adspecies, and the adsorbed oxygen were more active
468 than bulk lattice oxygen for NH_3 oxidation.

469

470 **Acknowledgements**

471 This work was sponsored financially by the National Nature Science Foundation
472 of China (No. 21377016, 21577014), the Natural Science Foundation of Liaoning
473 Province (No.2014020011), the Doctoral Fund of Shandong Province (BS2015HZ003)
474 and the Open Foundation of Key Laboratory of Industrial Ecology and Environmental
475 Engineering, MOE (KLIEEE-15-05).

References

1. L. Chmielarz, M. Jabłońska, A. Strumiński, Z. Piwowarska, A. Węgrzyn, S. Witkowski and M. Michalik, *Appl. Catal. B: Environ.*, 2013, **130-131**, 152.
2. S. M. Lee, H. H. Lee and S. C. Hong, *Appl. Catal. A: Gen.*, 2014, **470**, 189.
3. C. M. Hung, *Powder Technol.*, 2009, **196**, 56.
4. L. Chmielarz, P. Kuśtrowski, A. Rafalska-Łasocha and R. Dziembaj, *Appl. Catal. B: Environ.*, 2005, **58**, 235.
5. L. Chmielarz, A. Węgrzyn, M. Wojciechowska, S. Witkowski and M. Michalik, *Catal. Lett.*, 2011, **141**, 1345.
6. X. Cui, J. Zhou, Z. Ye, H. Chen, L. Li, M. Ruan and J. Shi, *J. Catal.*, 2010, **270**, 310.
7. J. C. Lou, C. M. Hung and S. F. Yang, *J. Air & Waste Manage. Assoc.*, 2004, **54**, 68.
8. Z. Wang, Z. Qu, X. Quan and H. Wang, *Appl. Catal. A: Gen.*, 2012, **411-412**, 131.
9. W. Chen, Y. Ma, Z. Qu, Q. Liu, W. Huang, X. Hu and N. Yan, *Environ. Sci. Technol.*, 2014, **48**, 12199.
10. Z. Wang, Z. Qu, X. Quan, Z. Li, H. Wang and R. Fan, *Appl. Catal. B: Environ.*, 2013, **134–135**, 153.
11. A. V. Kucherov, C. P. Hubbard, T. N. Kucherova and M. Shelef, *Appl. Catal. B: Environ.*, 1996, **7**, 285.
12. R. Bulánek, B. Wichterlová, Z. Sobalík and J. Tichý, *Appl. Catal. B: Environ.*, 2001, **31**, 13.

13. G. A. El-Shobaky, H. M. A. Hassan, N. S. Yehia and A. R. A. A. Badawy, *J. Non-Cryst. Solids*, 2010, **356**, 32.

14. A. Bueno-López, K. Krishna and M. Makkee, *Appl. Catal. A: Gen.*, 2008, **342**, 144.

15. A. Y. Khodakov, W. Chu and P. Fongarland, *Chem. Rev.*, 2007, **107**, 1692.

16. B. Jiang, Y. Liu and Z. Wu, *J. Hazard. Mater.*, 2009, **162**, 1249.

17. K. Dyrek and M. Che, *Chem. Rev.*, 1997, **97**, 305.

18. A. Martínez-Arias, M. Fernández-García, V. Ballesteros, L. N. Salamanca, J. C. Conesa, C. Otero and J. Soria, *Langmuir*, 1999, **15**, 4796.

19. C. J. G. Van Der Grift, A. F. H. Wielers, B. P. J. Jogh, J. Van Beunum, M. De Boer, M. Versluijs-Helder and J. W. Geus, *J. Catal.*, 1991, **131**, 178.

20. M. A. Gómez-García, V. Pitchon and A. Kiennemann, *Environ. Sci. Technol.*, 2005, **39**, 638.

21. B. M. Reddy, P. Bharali, P. Saikia, S. E. Park, M. W. E. Van Den Berg, M. Muhler and W. Grünert, *J. Phys. Chem. C*, 2008, **112**, 11729.

22. J. Giménez-Mañogil, A. Bueno-López and A. García-García, *Appl. Catal. B: Environ.*, 2014, **152-153**, 99.

23. L. Xu, H. Song and L. Chou, *Int. J. Hydrogen Energy*, 2012, **37**, 18001.

24. T. Sukonket, A. Khan, B. Saha, H. Ibrahim, S. Tantayanon, P. Kumar and R. Idem, *Energy Fuels*, 2011, **25**, 864.

25. A. P. Jia, G. S. Hu, L. Meng, Y. L. Xie, J. Q. Lu and M.-F. Luo, *J. Catal.*, 2012, **289**, 199.

26. L. Xie, F. Liu, L. Ren, X. Shi, F. S. Xiao and H. He, *Environ. Sci. Technol.*, 2013, **48**, 566.

27. A. A. Kaïs, A. Bennani, C. F. Aïssi, G. Wrobel and M. Guelton, *J. Chem. Soc., Faraday Trans.*, 1992, **88**, 1321.

28. G. R. Rao, H. R. Sahu and B. G. Mishra, Colloids Surfaces A. 2003, **220**, 261.

29. A. Aboukais, A. Bennani, C. F. Aissi, M. Guelton and J. C. Vedrine, *Chem. Mater.* 1992, **4**, 977.

30. A. Aboukaïs, A. Bennani, C. F. Aïssi, G. Wrobel, M. Guelton and J. C. Vedrine, *J. Chem. Soc., Faraday Trans.*, 1992, **88**, 615.

31. F. B. Noronha, E. C. Fendley, R. R. Soares, W. E. Alvarez and D. E. Resasco, *Chem. Eng. J.*, 2001, **82**, 21.

32. X. Liu, K. Zhou, L. Wang, B. Wang and Y. Li, *J. Am. Chem. Soc.*, 2009, **131**, 3140.

33. S. Tsunekawa, K. Ishikawa, Z. Q. Li, Y. Kawazoe and A. Kasuya, *Phys. Rev. Lett.*, 2000, **85**, 3440.

34. G. Avgouropoulos and T. Ioannides, *Appl. Catal. B: Environ.*, 2006, **67**, 1.

35. L. Kundakovic and M. Flytzani-Stephanopoulos, *Appl. Catal. A: Gen.*, 1998, **171**, 13.

36. F. Wang, H. Dai, J. Deng, G. Bai, K. Ji and Y. Liu, *Environ. Sci. Technol.*, 2012, **46**, 4034.

37. J. Deng, H. Dai, H. Jiang, L. Zhang, G. Wang, H. He and C. T. Au, *Environ. Sci. Technol.*, 2010, **44**, 2618.

38. R. Zhang, H. Alamdari and S. Kaliaguine, *J. Catal.*, 2006, **242**, 241.

39. A. Machocki, T. Ioannides, B. Stasinska, W. Gac, G. Avgouropoulos, D. Delimaris, W. Grzegorczyk and S. Pasieczna, *J. Catal.*, 2004, **227**, 282.

40. S. He, C. Zhang, M. Yang, Y. Zhang, W. Xu, N. Cao and H. He, *Sep. Purif. Technol.*, 2007, **58**, 173.

41. M. Yang, C. Wu, C. Zhang and H. He, *Catal. Today*, 2004, **90**, 263.

42. L. Lietti, G. Ramis, G. Busca, F. Bregani and P. Forzatti, *Catal. Today*, 2000, **61**, 187.

43. P. Fabrizioli, T. Buergi and A. Baiker, *J. Catal.*, 2002, **207**, 88.

44. R. Long and R. Yang, *J Catal.*, 2002, **207**, 158.

45. L. Gang, B. Anderson, J. Van Grondelle and R. Van Santen, *Catal. Today*, 2000, **61**, 179.

46. S. D. Lin, A. C. Gluhoi and B. E. Nieuwenhuys, *Catal. Today*, 2004, **90**, 3.

47. M. S. Kim, D. W. Lee, S. H. Chung, Y. K. Hong, S. H. Lee, S. H. Oh, I. H. Cho and K. Y. Lee, *J. Hazard. Mater.*, 2012, **237-238**, 153.

48. H. Sjövall, L. Olsson, E. Fridell and R. J. Blint, *Appl. Catal. B: Environ.*, 2006, **64**, 180.

49. S. Royer, A. Van Neste, R. Davidson, S. McIntyre and S. Kaliaguine, *Ind. Eng. Chem. Res.*, 2004, **43**, 5670.

50. G. Qi, J. E. Gatt and R. T. Yang, *J. Catal.*, 2004, **226**, 120.

51. M. Amblard, R. Burch and B. Southward, *Appl. Catal. B: Environ.*, 1999, **22**, 159.

52. W. K. Fung, M. Claeys and E. van Steen, *Catal.Lett.*, 2012, **142**, 445.

53. L. Gang, B. Anderson, J. Van Grondelle and R. Van Santen, *Appl. Catal. B: Environ.*, 2003, **40**, 101.

54. L. Zhang and H. He, *J. Catal.*, 2009, **268**, 18.

55. R. Q. Long and R. T. Yang, *Chem. Commun.*, 2000, 1651.

56. A. Łamacz, A. Krztoń and G. Djéga-Mariadassou, *Catal. Today*, 2011, **176**, 126.

57. B. Levasseur and S. Kaliaguine, *Appl. Catal. B: Environ.*, 2009, **88**, 305.

58. Y. C. Wei, J. Liu, Z. Zhao, A. J. Duan and G. Y. Jiang, *J. Catal.*, 2012, **287**, 13.

59. A. A. Kaïs, R. Bechara, D. Ghoussoub, C. F. Aïssi, M. Guelton and J. P. Bonnelle, *J. Chem. Soc., Faraday Trans.*, 1991, **87**, 631.

60. G. Wagner, R. Schumacher and S. Friedberg, *Physical Review*, 1966, **150**, 226.

61. G. F. Kokoszka, H. C. Allen Jr and G. Gordon, *J. Chem. Phys.*, 2004, **46**, 3013.

62. D. C. Sayle, S. A. Maicaneanu and G. W. Watson, J. *Am. Chem. Soc.*, 2002, **124**, 11429.

580

581 **Table 1 Physicochemical properties, $T_{50\%}$, $T_{90\%}$, Cu dispersion and TOF for NH_3**

582 **oxidation at 180°C**

Catalysts	BET (m^2/g)	V (cm^3/g)	P (nm)	$T_{50\%}$ (°C)	$T_{90\%}$ (°C)	Cu dispersion (D_{Cu}) (%)	TOF (h^{-1})
Cu-Ce-Zr (SOL)	95.64	0.15	3.77	160	190	53.3	1.33
Cu-Ce-Zr (HP)	84.85	0.20	3.80	190	230	51.7	1.03
Cu/CeO_2-ZrO_2 (IW)	124.3	0.25	6.58	220	260	49.3	0.85
Cu/Ce-Zr (IW)	117.4	0.31	9.64	245	290	43.1	0.72

583

584

585 **Table 2 Comparison of the complete conversion temperature ($T_{100\%}$) over different catalysts in the literatures for NH_3 oxidation**

Catalysts	Composition of testing gas	Conditions	$T_{100\%}$ (°C)	N_2 selectivity (%)	References
Cu-Ce-Zr (SOL)	1000 ppm NH_3, 10% O_2, He balance	40000 h^{-1}	220	98	This study
CuO/RuO_2	1000 ppm NH_3, 2% O_2, He balance	75000 ml h^{-1} g^{-1}	180	97	6
$CuO\text{-}CeO_2$ (6 wt% Cu)	1000 ppm NH_3, 10% O_2, He balance	40000 h^{-1}	250	95	10
10 wt% Cu/Al_2O_3	1% vol NH_3, 10%O_2, He balance	0.8 g	350	98	41
10 wt% Cu/TiO_2	400 ppm NH_3, 10% O_2, He balance	50000 h^{-1}	275	95	40
12 wt% MoO_3/SiO_2	960 ppm NH_3, 0.9% O_2, 0.15% Ar, He balance	0.128 g, 120 ml/min	500	71	42
6.1 wt% Mn/SiO_2	2000 ppm NH_3, 2% O_2, He balance	24000 h^{-1}	325	30	43
			1.01 h^{-1}[a]		
3.5 wt% Fe/TiO_2	1000 ppm NH_3, 2% O_2, He balance	200000 h^{-1}	400	91	44
1.46 wt% Pt-ZSM-5	1000 ppm NH_3, 2% O_2, He balance	1.2×10^{-3} g min ml^{-1}	225	65	47
1.2 wt% Ir/Al_2O_3	1000 ppm NH_3, 10% O_2, He	50 ml/min, 0.1 g	200	84	45
4.7 wt % Au/Al_2O_3	2 vol % NH_3, 2% O_2, He balance	30 ml/min	380	—	46

586 [a] TOF of Mn/SiO_2 catalyst at 230°C.

Table 3 Surface compositions, the relative desorption amount of O_2 and NH_3

Catalysts	Cu/Ce		Surface content (%)[b]		Relative content[c]		Relative desorption amount[d]	
	Bulk[a]	Surface[b]	$Ce^{3+}/(Ce^{3+}+Ce^{4+})$	O_{ads}/O_{latt}	total O_2	β-O_2	total amount	chemisorbed
Cu-Ce-Zr (SOL)	0.20	0.87	15.5	1.72	1.00	1.00	1.00	1.00
Cu-Ce-Zr (HP)	0.19	0.71	11.1	1.25	0.72	0.71	0.72	0.69
Cu/CeO_2-ZrO_2 (IW)	0.21	0.67	10.0	0.87	0.67	0.64	0.67	0.62
Cu/Ce-Zr (IW)	0.20	0.59	7.5	0.62	0.49	0.46	0.65	0.58

[a] Calculated by ICP.

[b] Calculated by XPS.

[c] Calculated by O_2-TPD.

[d] Calculated by NH_3-TPD.

Figure captions

Fig. 1 XRD patterns of catalysts prepared by different methods.

Fig. 2 (A) H_2-TPR profiles of catalysts prepared by different methods and (B) the quantitative analysis results of H_2-TPR: a Cu-Ce-Zr (SOL); b Cu-Ce-Zr (HP); c Cu/CeO_2-ZrO_2 (IW); d Cu/Ce-Zr (IW).

Fig. 3 (A) EPR spectra recorded at room temperature for Cu-Ce-Zr (SOL) catalyst and (B) EPR spectra of different catalysts: a Cu-Ce-Zr (SOL); b Cu-Ce-Zr (HP); c Cu/CeO_2-ZrO_2 (IW); d Cu/Ce-Zr (IW).

Fig. 4 (A) Ce 3d, (B) Cu 2p and (C) O 1s XPS spectra of a Cu-Ce-Zr (SOL); b Cu-Ce-Zr (HP); c Cu/CeO_2-ZrO_2 (IW); d Cu/Ce-Zr (IW).

Fig. 5 O_2-TPD profiles of different catalysts: a Cu-Ce-Zr (SOL); b Cu-Ce-Zr (HP); c Cu/CeO_2-ZrO_2 (IW); d Cu/Ce-Zr (IW).

Fig. 6 NH_3 conversion (A) and N_2 selectivity over catalysts prepared by different methods.

Fig. 7 TOF of NH_3 oxidation with the reaction temperature over the catalysts prepared by different methods.

Fig. 8 Influence of H_2O, SO_2, CO_2 and hytrothermal treatment on NH_3 conversion over Cu-Ce-Zr (SOL) catalyst.

Fig. 9 NH_3-TPD profiles over different catalysts.

Fig. 10 *In-situ* EPR spectra recorded at room temperature of Cu-Ce-Zr (SOL) samples during different treatment: a fresh Cu-Ce-Zr (SOL); b after adsorption of NH_3 at room temperature over fresh Cu-Ce-Zr (SOL); c after treatment by He at 230^{o}C over

621 Cu-Ce-Zr (SOL); d after treatment of NH_3 at 230^oC over Cu-Ce-Zr (SOL); e after
622 treatment of O_2 at 230^oC following by step d; f after treatment of NH_3 at 230^oC
623 following by step e.

624 **Fig. 11** (A) Effect of O_2 concentration on the NH_3 conversion over Cu-Ce-Zr (SOL)
625 catalyst at 220^oC (Inset: NH_3 conversion in the presence/absence of O_2 as a function
626 of time at 220^oC); (B) The in-situ O_2-TPD profiles of O_2-A, O_2-B, O_2-C and O_2-D.

627 **Fig. 12** The reaction models of NH_3 oxidation on Cu-Ce-Zr (SOL) catalyst.

628

Fig. 1

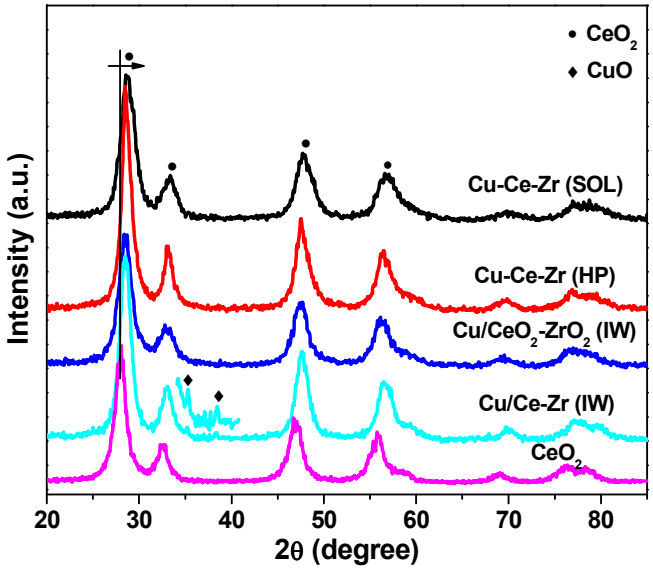

Fig. 2

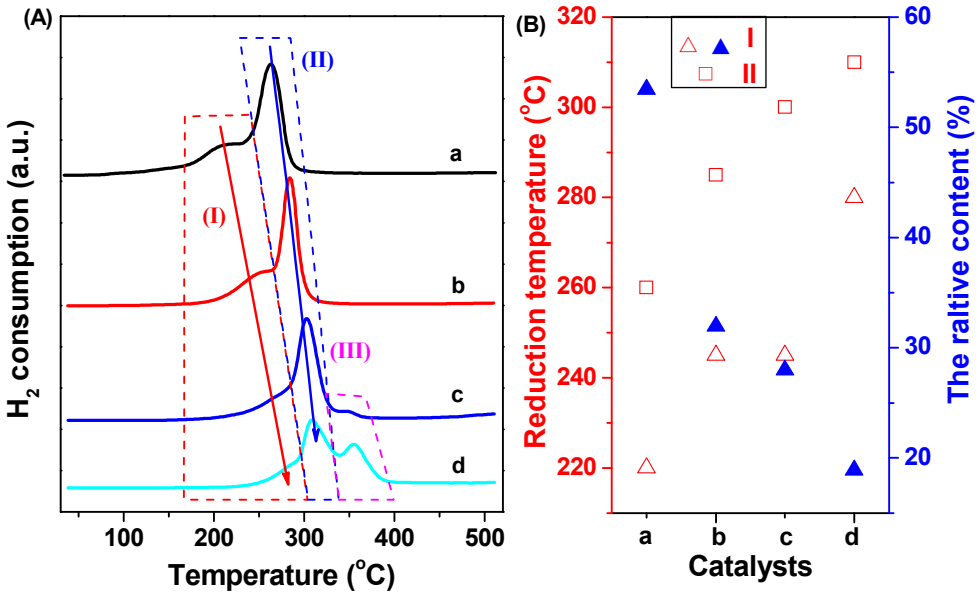

643

644 **Fig. 3**

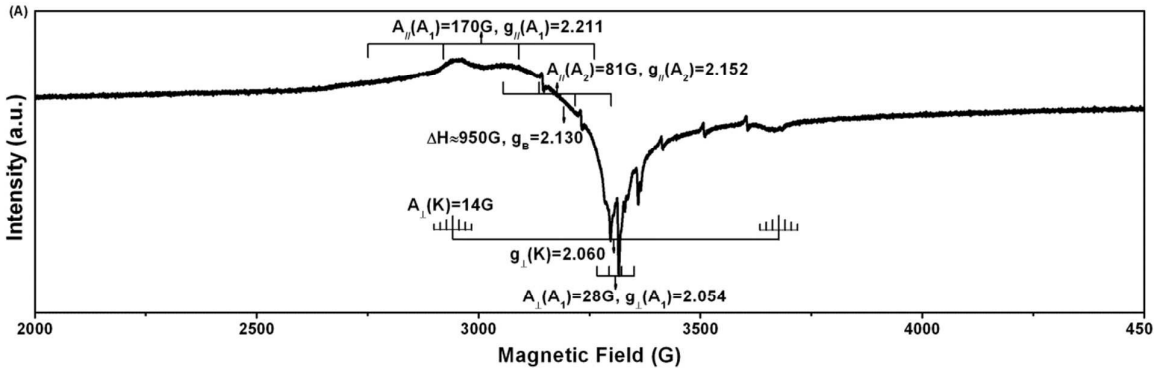

645

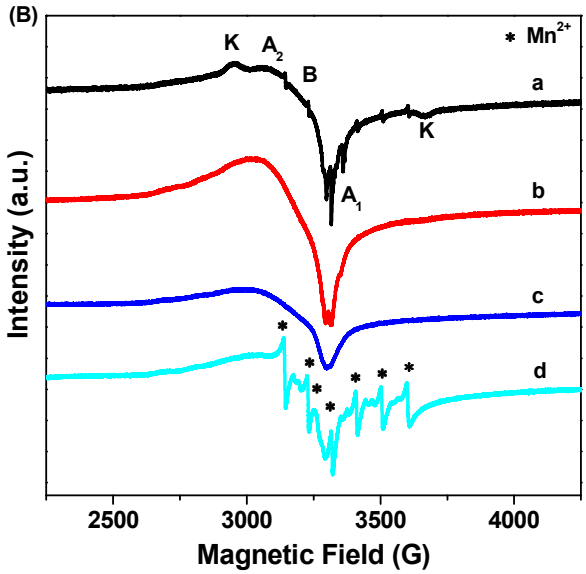

646

647

648

649

650

651

652

653

654 **Fig. 4**

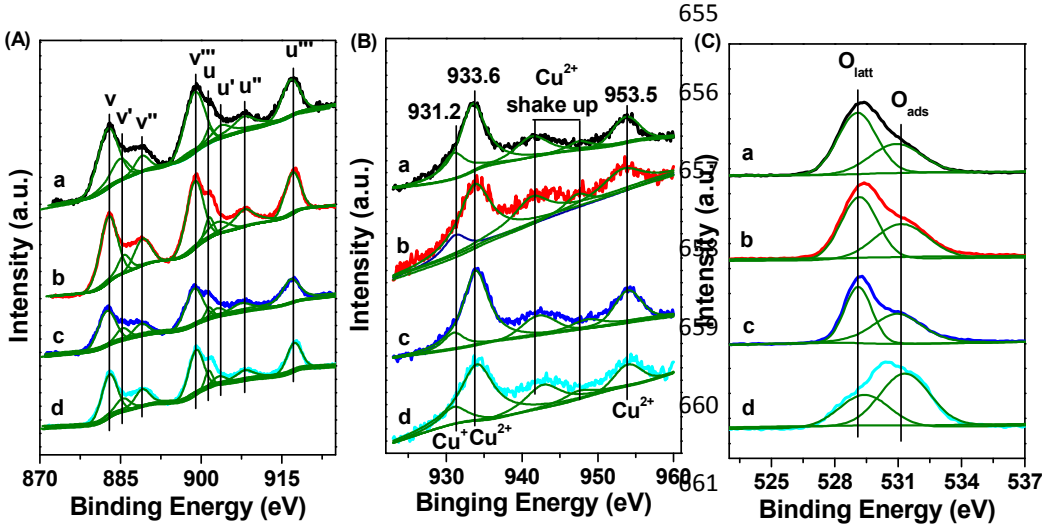

655 656 657 658 659 660 661 662

663

664 **Fig. 5**

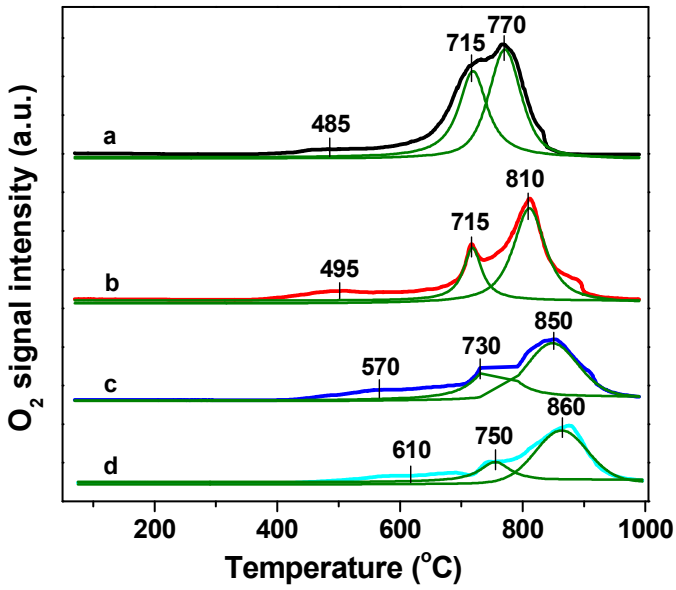

665

666

667

668 **Fig. 6**

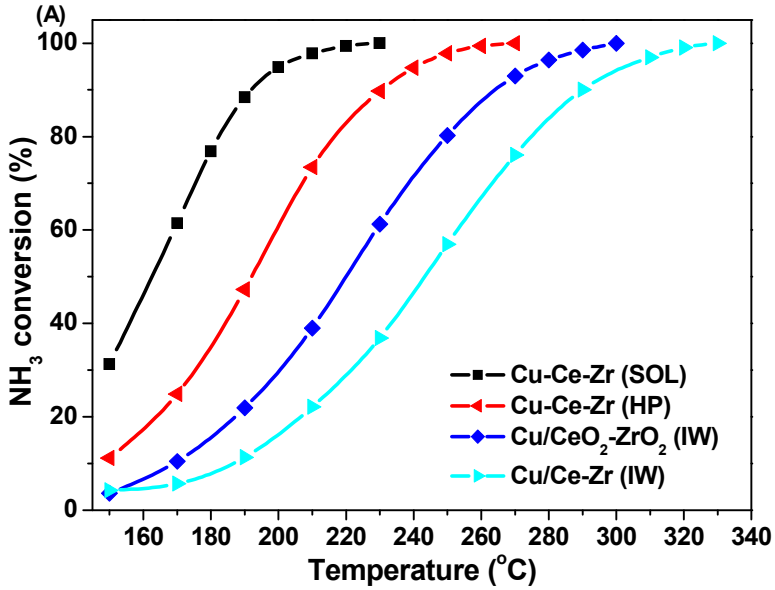

669

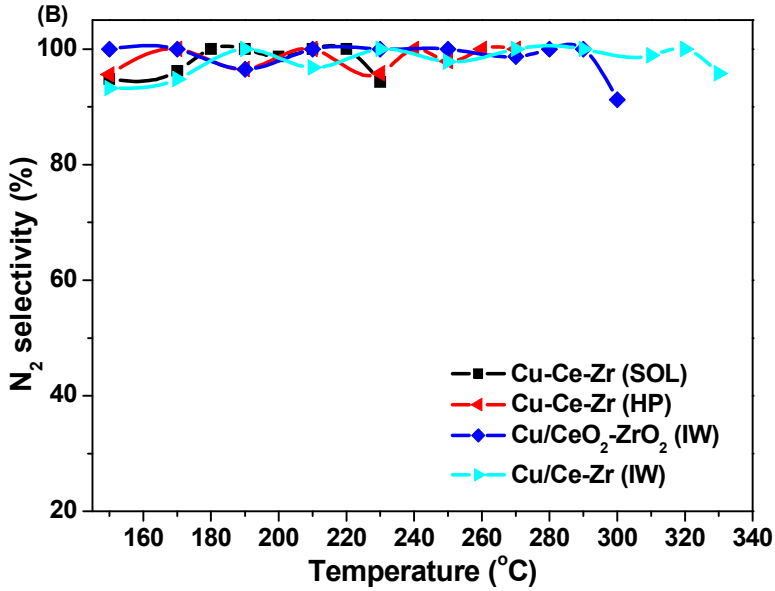

670

671

672

673 **Fig. 7**

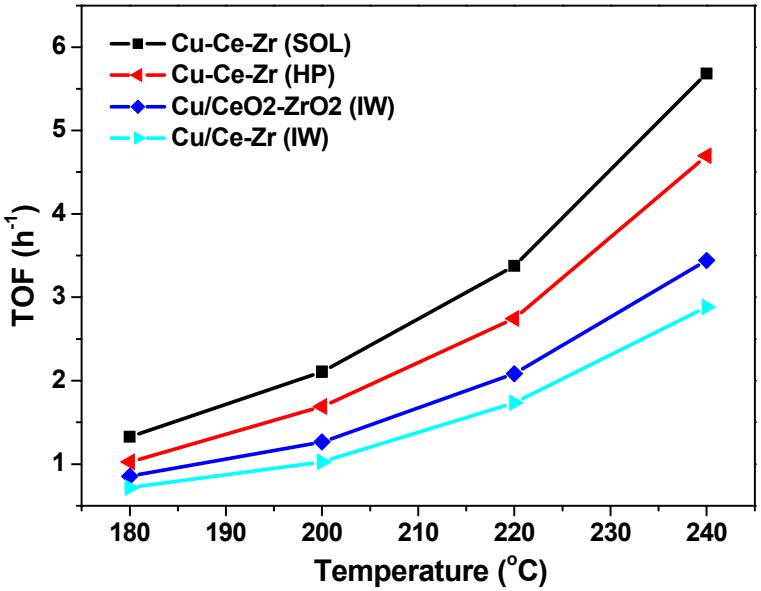

674

675 **Fig. 8**

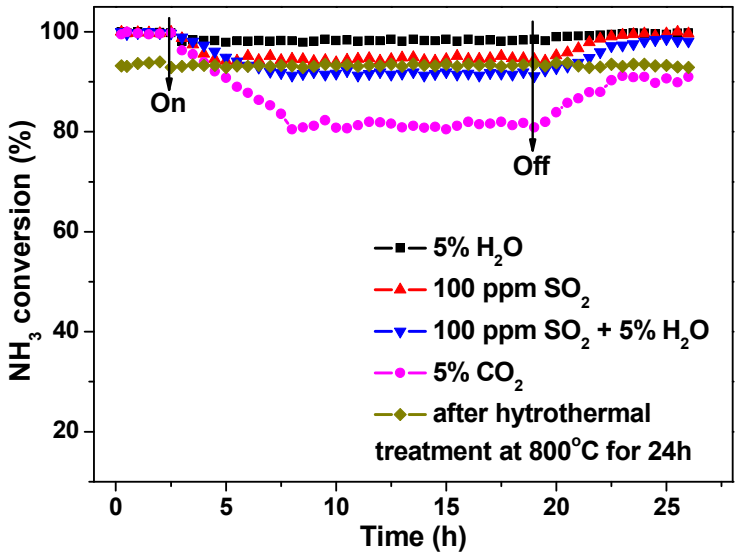

676

677

678

679 **Fig. 9**

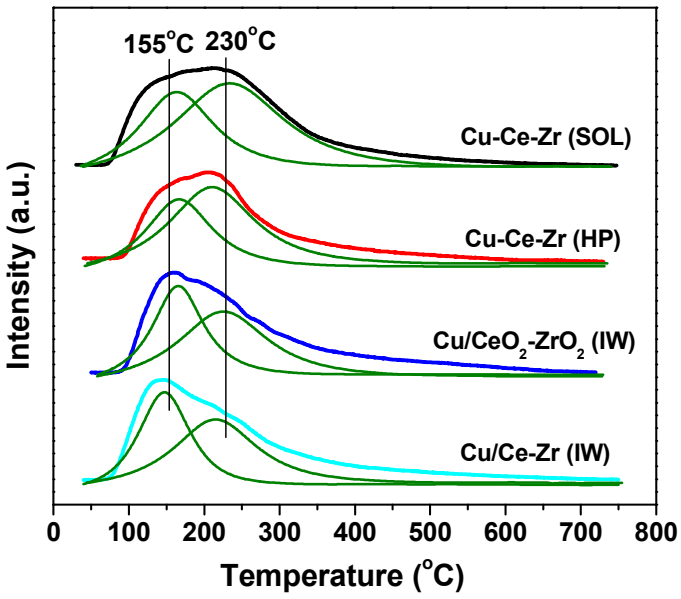

680

681 **Fig. 10**

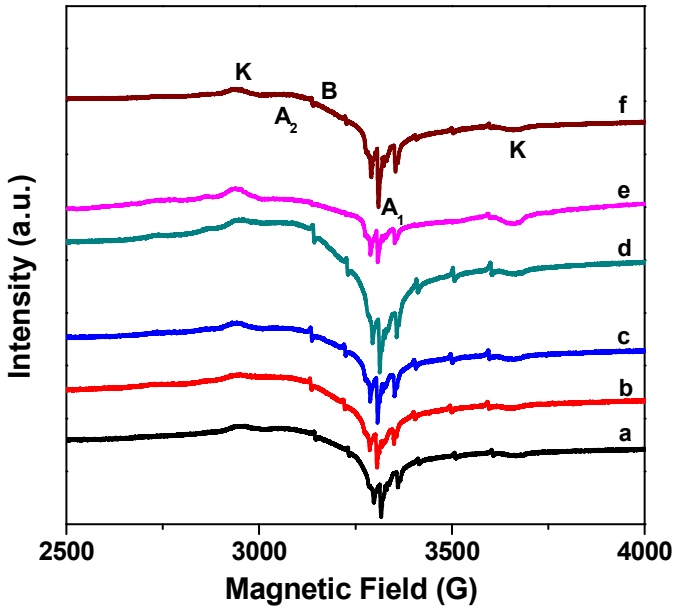

682

683

684 **Fig. 11**

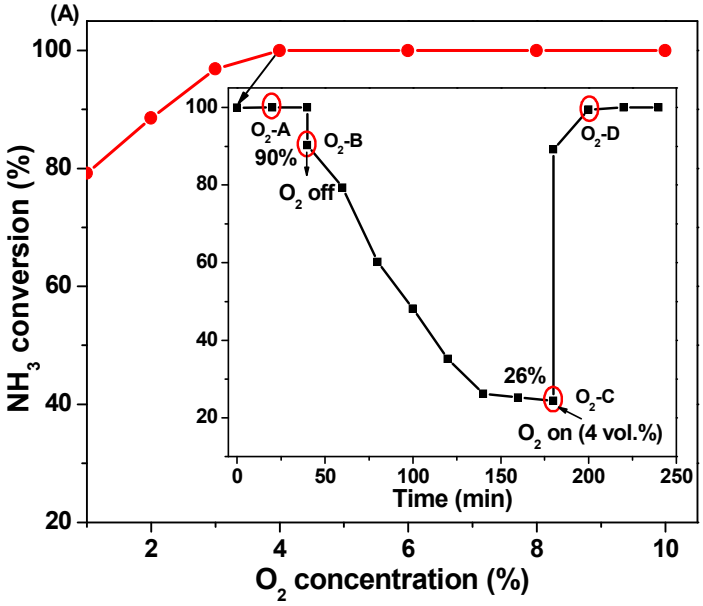

685

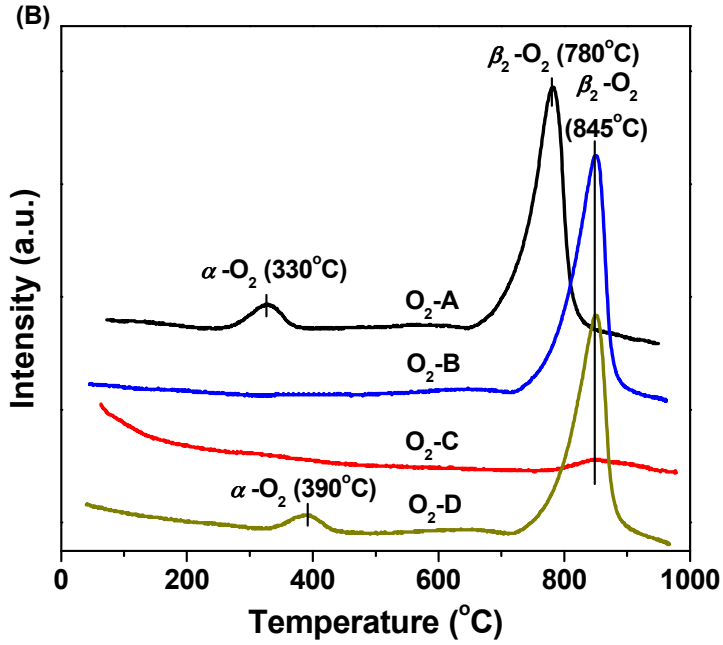

686

687

688

689 **Fig. 12**

690

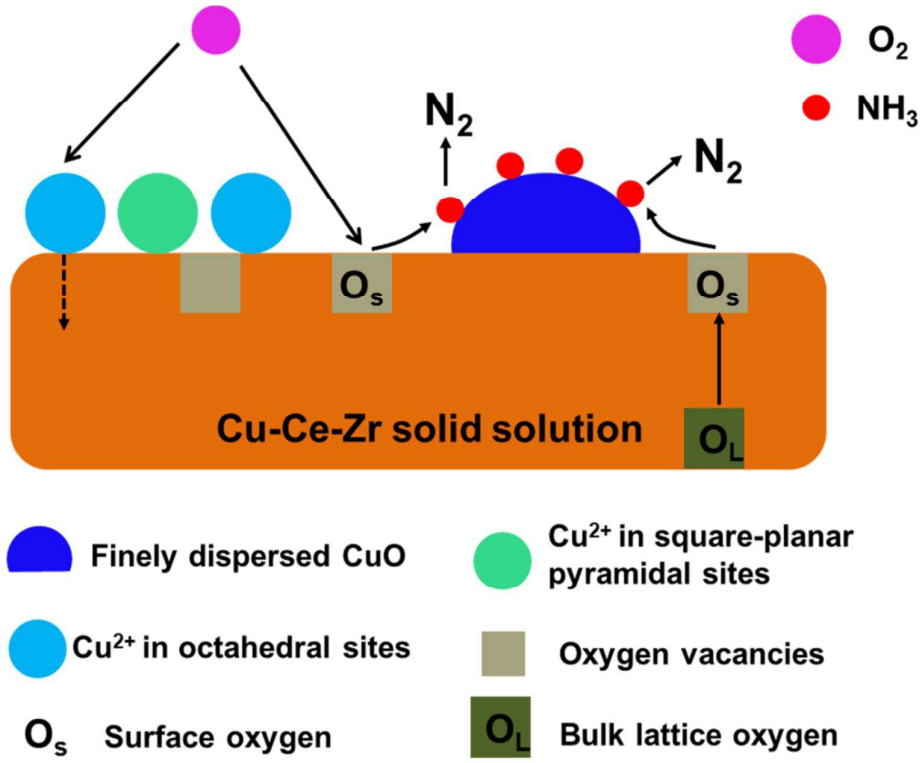

691

Graphical abstract